

An efficient feedback calibration algorithm for direct imaging radio telescopes

Adam P. Beardsley,¹★ Nithyanandan Thyagarajan,¹ Judd D. Bowman¹
and Miguel F. Morales²

¹Arizona State University, School of Earth and Space Exploration, Tempe, AZ 85287, USA

²University of Washington, Department of Physics, Seattle, WA 98195, USA

Accepted XXX. Received YYY; in original form ZZZ

ABSTRACT

We present the E-field Parallel Imaging Calibration (EPICal) algorithm, which addresses the need for a real-time calibration method for direct imaging radio astronomy correlators. Direct imaging involves a spatial fast Fourier transform of antenna voltages, alleviating the harsh $O(N_a^2)$ computational scaling to a more gentle $O(N_a \log_2 N_a)$, which can save orders of magnitude in computation cost for next generation arrays consisting of hundreds to thousands of antennas. However, because signals are mixed in the correlator, gain correction must be applied on the front end. We develop the EPICal algorithm to form gain solutions in real time without ever forming visibilities. This method scales as the number of antennas, and produces results comparable to those from visibilities. Through simulations and application to Long Wavelength Array data we show this algorithm is a feasible solution for next generation instruments.

Key words: instrumentation: interferometers – techniques: image processing – techniques: interferometric

1 INTRODUCTION

In order to satisfy the survey speeds required for precision cosmology as well as searches for fast radio transients, radio astronomy is undergoing a paradigm shift toward interferometers consisting of hundreds to thousands of small, widefield antennas. Many arrays with this design are already built or under construction including the Hydrogen Epoch of Reionization Array¹ (HERA), the Murchison Widefield Array (MWA; Tingay et al. 2013; Bowman et al. 2013), the Precision Array for Probing the Epoch of Reionization (PAPER; Parsons et al. 2010), the LOw Frequency ARray (LOFAR; van Haarlem et al. 2013), the Canadian Hydrogen Intensity Mapping Experiment (CHIME; Bandura et al. 2014), the Long Wavelength Array (LWA; Ellingson et al. 2013), and the low frequency Square Kilometer Array (SKA1-Low Mellema et al. 2013).

Traditional radio correlators cross-multiply the voltage signals from all pairs of antennas, and the computation scales as the number of antennas squared, $O(N_a^2)$ (Bunton 2004). As the number of elements in future arrays grows, the computational cost will become prohibitively expensive, and exploring efficient correlator schemes is essential to enable next generation instruments (Lonsdale et al. 2000). Meanwhile, radio transient monitoring requires access to high time and frequency resolution data. For example, fast radio

bursts (FRBs) are highly unexplored at low frequencies (< 1 GHz), but are expected to occur on timescales $\Delta t \sim 1\text{--}10$ ms (Thornton et al. 2013). Recording the full visibility matrix for $N_a \gtrsim 10^3$ arrays at this timescale leads to extremely high data write rates.

Direct imaging correlators are a new variety of radio correlator which aim to alleviate both the computational strain of forming N_a^2 correlations and the high data throughput associated with short timescale science. This is done by performing a spatial fast Fourier transform (FFT) to image the antenna voltages, then squaring and averaging in time. This process scales as $O(N_g \log_2 N_g)$, where N_g is the number of grid points in the FFT (Morales 2011; Tegmark & Zaldarriaga 2009; Tegmark & Zaldarriaga 2010). For certain classes of telescopes, significantly those envisioned for next generation cosmology experiments, this scaling is a large improvement over the N_a^2 scaling of traditional methods. Furthermore, because images are generated online, the native output bandwidth will be lowered (assuming $N_g < N_a^2$), and has the potential to be lowered even further with online transient processing.

A handful of prototype direct imaging correlators have been tested on arrays including the Basic Element for SKA Training II (BEST-2) array (Foster et al. 2014), the Omniscope (Zheng et al. 2014), and an earlier pulsar timing experiment at GHz frequencies (Otoe et al. 1994; Daishido et al. 2000). Each of these are examples of so-called FFT correlators – a subclass of direct imaging correlators which rely on identical antennas with restricted placement, which allows the FFT to be performed without gridding. We recently

★ E-mail: Adam.Beardsley@asu.edu

¹ <http://reionization.org>

released the E-field Parallel Imaging Correlator (EPIC; [Thyagarajan et al. 2015a](#)), which is a software implementation of the Modular Optimal Frequency Fourier (MOFF; [Morales 2011](#)) imaging algorithm. This architecture leverages the software holography/A-transpose framework to grid electric field data streams before performing the spatial FFT, allowing for an optimal map without placing constraints on array layout or requiring identical antennas ([Morales & Matejek 2009](#); [Bhatnagar, S. et al. 2008](#); [Tegmark 1997](#)).

A challenge common to all direct imaging algorithms is calibration of the antenna gains. Traditionally, pair-wise visibilities are written to disk and used to calibrate offline. However, a direct imaging correlator mixes the signals from all antennas before averaging and writing to disk, making calibration a requirement at the front end (**need to make this distinction more clear by pointing where exactly calibration happens in a X-based system and MOFF**). Previous solutions have involved applying calibration solutions generated from a parallel FX correlator ([Zheng et al. 2014](#); [Foster et al. 2014](#)), or integrating a dedicated FX correlator which periodically formed the full visibility matrix to solve for gains ([Wijnholds & van der Veen 2009](#); [de Vos et al. 2009](#)). While these solutions were sufficient to enable the exploration of FFT correlators and beam-formers, they will not scale to future arrays with $N_a \gtrsim 10^3$.

Here we present the E-field Parallel Imaging Calibration (EPI-Cal) algorithm – a novel solution to the calibration problem, which can be integrated into direct imaging correlators and scales only as the number of antennas, $O(N_a)$. This method uses a correlation of the uncalibrated antenna signal stream with an output image pixel from the backend of the correlator to solve for the complex gains of the antennas. Because the calibration must be applied before gridding and imaging, our solution requires an iterative approach where the data from one time series is used to update the gains which are applied to the following time series. An example implementation of the algorithm is available with the EPIC software package².

We establish the mathematical framework and derive the calibration algorithm in §2. We then demonstrate the algorithm in simulations in §3, and apply to a sample LWA data set in §4. Then we discuss the noise properties of the resulting gain solutions in §5. Finally we conclude and discuss potential extensions to the algorithm in §6.

2 MATHEMATICAL FRAMEWORK

We begin by establishing the mathematical framework for the calibration problem. We derive the calibration solutions for the MOFF algorithm (adopting the notation of [Thyagarajan et al. 2015a](#)), but note the result is easily extended to FFT correlator algorithms by removing the gridding step.

The electric field incident on the ground, $\tilde{E}(\mathbf{r}, f, t)$, is related to the sky electric field, $E(\hat{\mathbf{s}}, f, t)$, through a Fourier transform.

$$\tilde{E}(\mathbf{r}, f, t) = \int E(\hat{\mathbf{s}}, f, t) e^{-2\pi i \mathbf{r} \cdot \hat{\mathbf{s}}} d^2 \hat{\mathbf{s}} \quad (1)$$

Here $\hat{\mathbf{s}}$ denotes the sine-projected unit vector for the sky angle, \mathbf{r} is the observer’s location (measured in wavelengths relative to an arbitrary origin), and f and t denote the frequency and time dependence, respectively. We will encounter several quantities which we attempt to estimate. We distinguish the “true” values with a superscript T , while the estimates are denoted with a prime. We define the

true antenna signal as a convolution of the antenna voltage pattern, \tilde{W} , with the electric field on the ground.

$$\tilde{E}_a^T(f, t) \equiv \int \tilde{W}_a(\mathbf{r} - \mathbf{r}_a) \tilde{E}(\mathbf{r}, f, t) d^2 \mathbf{r} \quad (2)$$

The subscript a labels the antenna, and \mathbf{r}_a is the location of antenna a .

We next model the measured, uncalibrated electric field as a multiplicative complex gain and an additive noise term applied to the true antenna electric field.

$$\tilde{E}_a(f, t) = g_a^T(f, t) \tilde{E}_a^T(f, t) + \tilde{n}_a(f, t) \quad (3)$$

Note that this quantity is neither a true or estimated value. The noise term is strictly receiver noise – noise introduced by the instrument. Any sky noise is implicitly included in the time dependence of the sky electric field. As the noise of modern low frequency arrays is heavily dominated by sky noise, we will neglect \tilde{n}_a for now, but will inspect its effects at the end of this section.

The goal of our calibration algorithm will be to estimate the antenna gains. We will assume the gains have no time dependence within the timescale of finding our solutions. Furthermore, we will treat each frequency channel independently, and drop the f to simplify notation.

The MOFF algorithm next calls for a calibration. We will assume we have formed an estimate of the gains after n iterations of a calibration loop, and derive an updated **estimate for the $(n + 1)$ -th iteration**. How the calibration gain is applied can depend on the dominant source of the noise in the measurement. If the noise is dominated by sky fluctuations, the noise level is affected by the antenna gains so dividing by the complex gains will flatten the noise across antennas. However, if the noise is dominated in the receiver gain results in lower signal to noise for that antenna. Therefore, one should multiply by the conjugate of the gain to down weight it appropriately while removing the phase acquired. We will abstain from this choice for now, and instead use a multiplicative factor $h_a^{(n)}$ to represent the application of our n^{th} -loop estimate of the gain for antenna a :

$$\tilde{E}_a' = h_a^{(n)} \tilde{E}_a \quad (4)$$

where,

$$h_a^{(n)} = \begin{cases} 1/g_a^{(n)}, & \text{sky noise dominated} \\ g_a^{*(n)}, & \text{receiver noise dominated.} \end{cases} \quad (5)$$

A dirty image is next formed by gridding the calibrated fields with the antenna voltage pattern, Fourier transforming, squaring, and averaging in time. The estimated value for a pixel, $\hat{\mathbf{s}}_i$, can be expressed as

$$I'(\hat{\mathbf{s}}_i) = \left\langle \left| \frac{1}{N_a} \sum_i e^{2\pi i \mathbf{r}_i \cdot \hat{\mathbf{s}}_i} \sum_a \tilde{W}_a(\mathbf{r}_i - \mathbf{r}_a) h_a^{(n)} g_a^T \tilde{E}_a^T(t) \right|^2 \right\rangle_t \quad (6)$$

This is the final output of the MOFF correlator. However, for calibration purposes we will be interested in the electric field image just prior to squaring and averaging.

$$E'(\hat{\mathbf{s}}_i, t) = \frac{1}{N_a} \sum_i e^{2\pi i \mathbf{r}_i \cdot \hat{\mathbf{s}}_i} \sum_a \tilde{W}_a(\mathbf{r}_i - \mathbf{r}_a) h_a^{(n)} g_a^T \tilde{E}_a^T(t) \quad (7)$$

We can simplify this expression by exchanging the sums to transform

² <http://github.com/nithyanandan/EPIC>

the beam term into sky coordinates.

$$\begin{aligned}
 E'(\hat{s}_i, t) &= \frac{1}{N_a} \sum_a h_a^{(n)} g_a^T \tilde{E}_a^T(t) e^{2\pi i \hat{s}_i \cdot \mathbf{r}_a} \\
 &\quad \sum_i \tilde{W}_b(\mathbf{r}_i - \mathbf{r}_a) e^{2\pi i \hat{s}_i \cdot (\mathbf{r}_i - \mathbf{r}_a)} \\
 &= \frac{1}{N_a} \sum_a h_a^{(n)} g_a^T \tilde{E}_a^T(t) e^{2\pi i \hat{s}_i \cdot \mathbf{r}_a} W_a(\hat{s}_i)
 \end{aligned} \quad (8)$$

Next we move toward the feedback calibration outlined in [Morales 2011](#). There it was suggested to form a correlation of the uncalibrated antenna measurements with an image pixel from the output of the correlator. This is a statistically stationary quantity, which can be related to the sum of visibilities involving the antenna used in the correlation – exactly the sum needed to calibrate a simple sky of a single point source. However, we aim for a more generalized solution for arbitrarily complex sky models. We therefore study the full expression for the antenna-pixel correlation,

$$C_{a, \hat{s}_0}^{(n)} \equiv \langle \tilde{E}_a(t) E'^*(\hat{s}_0, t) \rangle_t, \quad (9)$$

where the superscript n again represents the quantity formed in the n^{th} calibration loop, and \hat{s}_0 is the pixel center nearest a bright calibrator of interest. The following will hold for any chosen pixel, \hat{s}_0 , though it is advantageous to choose a pixel which contains a bright source to achieve a high signal to noise.

Plugging equation 8 into equation 9, we find,

$$\begin{aligned}
 C_{a, \hat{s}_0}^{(n)} &= \left\langle g_a^T \tilde{E}_a^T(t) \frac{1}{N_a} \sum_b h_b^{*(n)} g_b^T \tilde{E}_b^T(t) e^{-2\pi i \hat{s}_0 \cdot \mathbf{r}_b} W_b^*(\hat{s}_0) \right\rangle_t \\
 &= \frac{g_a^T}{N_a} \sum_b h_b^{*(n)} g_b^T W_b^*(\hat{s}_0) e^{-2\pi i \hat{s}_0 \cdot \mathbf{r}_b} \langle \tilde{E}_a^T \tilde{E}_b^{*T} \rangle_t \\
 &= \frac{g_a^T}{N_a} \sum_b h_b^{*(n)} g_b^T W_b^*(\hat{s}_0) e^{-2\pi i \hat{s}_0 \cdot \mathbf{r}_b} \tilde{V}_{ab}^T
 \end{aligned} \quad (10)$$

where in the second step we group time-dependent terms, and in the third we define the true visibilities as the correlation between true antenna electric field measurements. It is easy to see from here that the net effect of including the receiver noise term, $\tilde{n}_a(f, t)$, will result in added noise on the true visibilities, including a bias on the auto-correlation terms. In principle a bias can result on any visibility from any noise correlations between antennas, but the implementation included in the EPIC software package restricts the noise term to include only the auto-correlation noise bias, and assumes baseline dependent noise **has** zero mean.

Finally, we find an update to our gain solution by assuming our current estimate of the gains, $g_b^{(n)}$, is approximately correct and substitute into the sum for the true gains. We also require model visibilities formed from sky and primary beam models in place of true visibilities.

$$g_a'^{(n+1)} = C_{a, \hat{s}_0}^{(n)} N_a \left[\sum_b h_b^{*(n)} g_b^{*(n)} W_b^*(\hat{s}_0) e^{-2\pi i \hat{s}_0 \cdot \mathbf{r}_b} \tilde{V}_{ab}^T \right]^{-1} \quad (11)$$

This equation is our prescription for estimating the antenna gains of a direct imaging array. The approach is iterative in nature, and requires a sky model. However, the sky model can be precomputed offline, and the online computation complexity scales only as $O(N_a)$ as we form a $C_{a, \hat{s}_0}^{(n)}$ for each antenna. In the case where $h_b = 1/g_b$ (typical calibration procedure for sky-noise dominated systems),

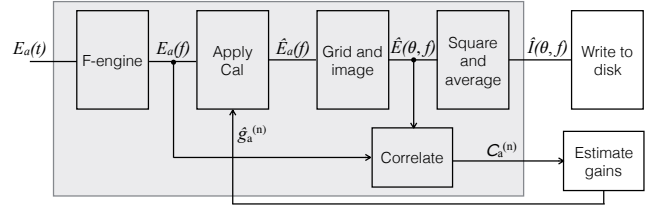


Figure 1. The general data flow of the MOFF correlator, with a feedback calibration loop. A pixel from the (unsquared) image is tapped out and correlated against the input antenna electric field signals to form $C_{a, \hat{s}_0}^{(n)}$ coefficients, which are used to estimate the antenna gains. These gain estimates are then fed back into the correlator to be applied to subsequent data, and the process is repeated. The gray box shows operations which must be done at high speed (before averaging in time), which white boxes show operations which can be performed “off-chip”. (I have some suggestions to tweak this figure.)

this simplifies slightly.

$$g_a'^{(n+1)} = C_{a, \hat{s}_0}^{(n)} N_a \left[\sum_b W_b^*(\hat{s}_0) e^{-2\pi i \hat{s}_0 \cdot \mathbf{r}_b} \tilde{V}_{ab}^T \right]^{-1} \quad (12)$$

While testing we found equation 11 resulted in oscillatory gain solutions as it was iterated, as is often the case in iterative minimization methods. To mitigate this we introduce a damping factor, $0 \leq \gamma < 1$, which is used to attenuate the gain update, effectively giving the solutions memory of previous iterations.

$$g_a^{(n+1)} = (1 - \gamma) g_a'^{(n+1)} + \gamma g_a^{(n)} \quad (13)$$

We found that while equation 11 does indeed converge on good solutions, the process is made faster by tuning the damping factor. While $g_a'^{(n+1)}$ is the best estimate of the gains after the n^{th} iteration, the damped version, $g_a^{(n+1)}$, is actually used in the iterative calibration loop. Once the loop converges the difference is a longer effective integration for the damped version (lower thermal noise) **(the last sentence is too condensed that it is not clear what you are trying to say)**.

We show schematically the process of calibrating a direct imaging correlator in figure 1. Computationally expensive steps that must be performed “on-chip” are shown inside the gray box. The uncalibrated antenna signals are tapped out after the F-engine and correlated against the output image pixel of interest (i.e., equation 9 is “on-chip”). The correlated values are then passed off-chip to estimate the gains using equation 11, and additional fitting if desired. The gains are then passed back to the correlator to update the calibration for subsequent data streams.

An important feature to note is that, like the MOFF-generated images themselves, equations 11 and 12 include the antenna auto-correlations (the sum is over *all* b , not excluding a). It can be difficult to perfectly model the noise bias from auto-correlations, which can often times be far brighter than the visibilities themselves. It can therefore be beneficial to subtract this term directly from $C_{a, \hat{s}_0}^{(n)}$, and exclude the $b = a$ term in the sum.

$$C_{a, \hat{s}_0}^{(n)} \rightarrow C_{a, \hat{s}_0}^{(n)} - \frac{1}{N_a} h_a^{*(n)} W_a^* e^{-2\pi i \hat{s}_0 \cdot \mathbf{r}_a} \langle |\tilde{E}_a|^2 \rangle_t \quad (14)$$

This requires generating these correlations, which again only scale as $O(N_a)$, and are generally useful for array diagnostics. **(What happened to the g_a^T term outside the sum? And why did you drop \hat{s}_0 in W_a^* ?)**

We conclude this section by connecting our calibration expression to that found in a visibility framework. In the limit of a single bright calibrating source at phase center, we can greatly simplify equations 10 and 11. We will assume the beams are normalized such that $W(0) = 1$. We can further drop the exponential phase terms because $\hat{s}_0 = 0$. We then absorb the true gains and gain corrections into the true visibilities in equation 10 to express as a sum of measured visibilities.

$$C_{a,0}^{(n)} \rightarrow \frac{1}{N_a} \sum_b h_b^{*(n)} \tilde{V}_{ab} \quad (15)$$

(It is not clear what happened to the g terms.)

We next plug this expression into equation 11 to find our simplified calibration solution for a single bright point source. Because our sky is a single bright point source, the model visibilities are simply the flux of the source, S_{src} .

$$g_a^{(n+1)} \rightarrow \left[\sum_b h_b^{*(n)} \tilde{V}_{ab} \right] \times \left[S_{\text{src}} \sum_b h_b^{*(n)} g_b^{*(n)} \right]^{-1} \quad (16)$$

This is simply a gain-weighted sum of the measured visibilities over the flux of the source, which is indeed the limiting result from a visibility approach, for example seen in Mitchell et al. 2008. The ability to recover the equivalent expression despite not actually forming the visibilities is a result of the fact that only sums over visibilities come into the FX solution, as was described in Morales 2011. We have confirmed the limiting case equivalence here, and will explore the more general case in more detail in § 5.

3 SIMULATION

We first demonstrate our calibration method through a controlled simulation. A complex gain is created for each antenna with random phase and amplitude, which is used to corrupt the simulated data stream, then we attempt to recover the gains using our calibration routine. The simulation software used is included in the EPIC package.

Our simulated signal consists of 10 random point sources with flux densities $0.5 \text{ Jy} \lesssim S \lesssim 1 \text{ Jy}$. For an antenna array we use the inner 51 antennas of the MWA layout (Beardsley et al. 2012), within a bounding box of 150 m. The antenna voltage pattern used is a 4.4 m square tophat on the ground. Because our algorithm treats frequency channels independently, we simulate only one channel. For context we treat this channel as a single 40 kHz, meaning each subsequent timestep is separated by $25 \mu\text{s}$.

For our unknown gains, we create a set of random numbers with amplitude 1 ± 0.25 (**replace with amplitude in range [0.75, 1.25]**), and completely random phase. These are our “true gains”, and we apply them to the frequency-domain simulated antenna electric fields as in equation 3. Our analysis is blind to these values until the end of the process to check accuracy. The gain estimates are initialized with unity, $g_a^{(0)} = 1$.

We next process and image 400 time steps (10 ms). We also form the correlations, $C_{a,\hat{s}_0}^{(0)}$, used in our calibration loop. The pixel used for the correlation is the source with the largest apparent flux (intrinsic flux attenuated by the primary beam). These correlation values are used to update the gain estimates, which in turn are used to calibrate the following 400 time steps. Through experimentation we found a damping factor of $\gamma = 0.35$ resulted in the quickest convergence in this simulation.

The calibration loop continues by updating the gain estimates

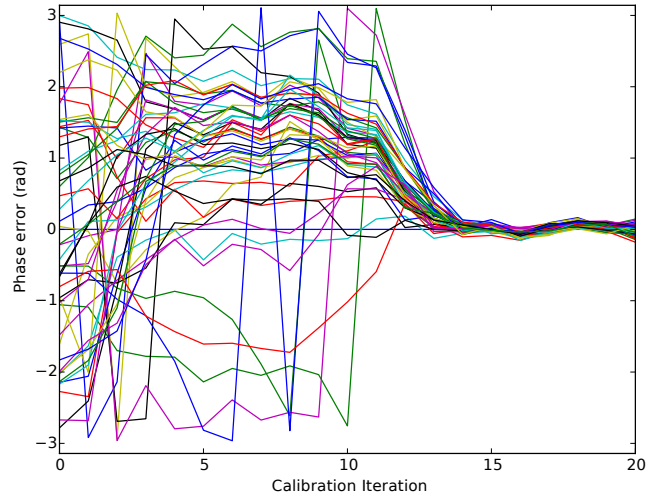


Figure 2. Phase error of gain estimates as a function of iteration for simulated calibration. The gains were initialized with random phases, but the calibration loop was able to recover the correct phases after about 15 iterations. Each line represents an antenna in our 51 MWA antenna sample.

every 400 time steps. The phases of our gain estimates are shown in figure 2 for 20 such iterations. The phase error plotted is the phase relative to the true gain for each antenna (various colored lines). One antenna was used as a reference to fix the absolute phase, so has zero phase error. The other 50 antennas are shown to have error spanning 2π initially, and after about 10 iterations lock into a solution, settling down to noise levels around iteration 15 (0.15 s). We stop the simulation when the updated gains trace the thermal noise of the simulated sources, which can be seen by the coherence of the 50 antenna gains after iteration 15.

The estimated gain amplitudes for the simulations are shown in figure 3. The quantity plotted is the magnitude of the estimated gains over the true gains, $|g_a^{(n)}/g_a^T|$, which places all antennas on the same scale. We can see the amplitudes converge toward their true values around the same time as the phases (iteration ~ 15). At the beginning of calibration we can see the value of the damping factor. At $n = 0$, a couple of gains are shown to have abnormally high amplitude estimates, notably one about 3.3 times its true value (red line). These unbalanced high estimates caused the entire set of gains to be under estimated at $n = 1$, even with a damping factor of 0.35. By $n = 5$ the unbalanced amplitudes have been damped out and the calibration continues. Without the damping factor, the oscillation seen in the first couple iterations would have been significantly larger and taken much longer to fade out. (**Add a sentence or two to explain the oscillation after convergence due to intrinsic source fluctuations.**)

Images created at the beginning of calibration and at the end are shown in figure 4. Each image is **obtained over** 10 ms integration, corresponding to all snapshot images created with a given set of gain estimates. The top panel shows the image produced with our initialized unity gains. Because the phases are completely random, the image is essentially noise with the primary beam evident. After 20 iterations, the image is far more clear, shown in the bottom panel. Each of the ten simulated sources are clearly visible, indicated with red circles.

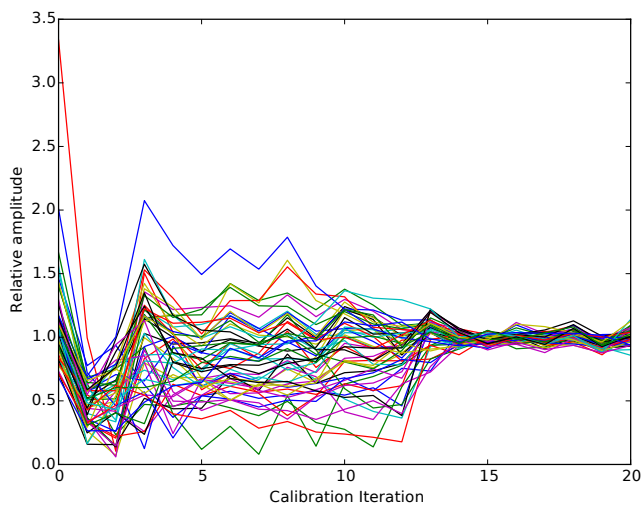


Figure 3. Gain estimate amplitudes as a function of iteration for simulated calibration. Again, each line represents an antenna in the 51 MWA antenna sample. The gain estimates were initialized randomly, while the true values were unity. After about 15 iterations we see the calibration loop has settled around the correct values, with only noise remaining.

4 APPLICATION TO LWA DATA

We next demonstrate our calibration algorithm using an observation from the LWA station in New Mexico. The data is from the LWA narrow-band transient buffer (TBN), with time ordered voltage data from 255 antennas within a core radius of 100 m. The central frequency is 74.03 MHz, with a bandwidth of 100 kHz and writeout timescale of 5.12 ms (frequency channel resolution of 195.3125 Hz). For this demonstration we limit ourselves to a single polarization.

After correcting for geometric cable delays, the instrument is naturally well calibrated, as was seen in the demonstration of the EPIC imager in Thyagarajan et al. 2015a. However, we will aim to improve further on this calibration using our algorithm.

We proceed by forming model visibilities. We model only two bright objects as point sources: Cyg A with flux 16611.68 Jy (Cohen et al. 2007); and Cas A with flux 17693.9 Jy (Kassim et al. 2007). Because the raw data is attenuated by the primary beam of the instrument, we also account for this in our model using beam values consistent with Hicks et al. (2012).

We made several choices while studying the behavior of the LWA data to improve our calibration. Through our previous imaging work, we noted that the flux scale of uncalibrated images was consistent with average gain amplitudes of 0.25. To allow the calibration to converge quickly we initialized our gain estimates at this level. We also found a boost in signal to noise is achieved easily by averaging frequency channels and assuming the gains are constant within a sub-band. Here we average solutions across 150 channels, or about 29 kHz. With a fractional bandwidth $B/f_0 = 3.9 \times 10^{-4} \ll 1$, we assume a smooth bandpass across the band. A damping factor of $\gamma = 0.7$ was adopted.

Finally, we found that seven antennas³ produced unstable gain solutions, and in fact corrupted the ensemble (specifically what is the ensemble exactly?). We therefore flagged these antennas in our analysis, resulting in a total of 248 antennas to calibrate. In each

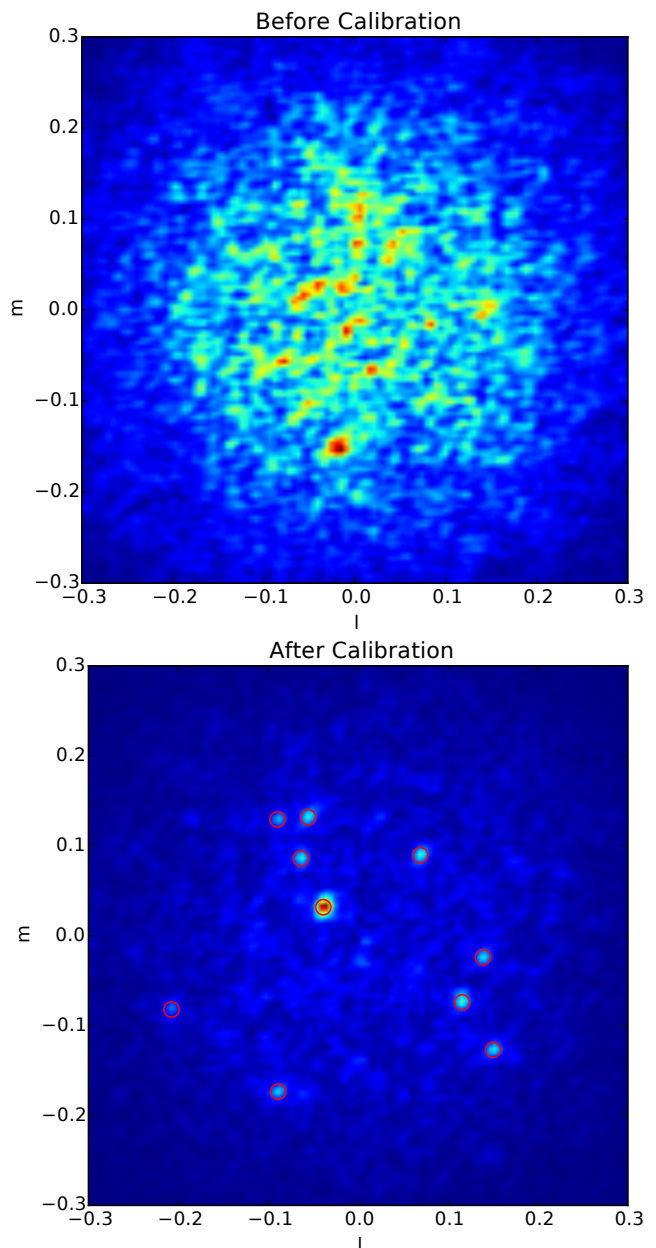


Figure 4. Images formed during simulated calibration. *Top:* An image generated from a single frequency channel and 10 ms integration after the gain estimates are randomized. As expected with random phases, the image is completely noisy, with the shape of the primary beam evident. *Bottom:* An image formed after calibration, again with a single frequency channel and 10 ms integration. The ten simulated (and modeled) point sources are easily visible, and highlighted with red circles.

calibration loop, we form C_{i,\hat{s}_0} , $i = 1, 2, \dots, N_a$ and update our gain estimates over 10 timestamps (51.2 ms). We iterate the loop 30 times for a total of 1.536 seconds. The results of this calibration experiment are shown in figures 5 – 7.

Figure 5 shows the phase of our gain estimates over 30 calibration iterations, again with each colored line representing a different antenna. Given the quality of uncalibrated image demonstrated in Thyagarajan et al. (2015a), it is a bit surprising to see the phase variation in our solutions. However, the phases are relatively flat af-

³ LWA antenna IDs 48, 85, 124, 148, 203, 217, and 244 were flagged.

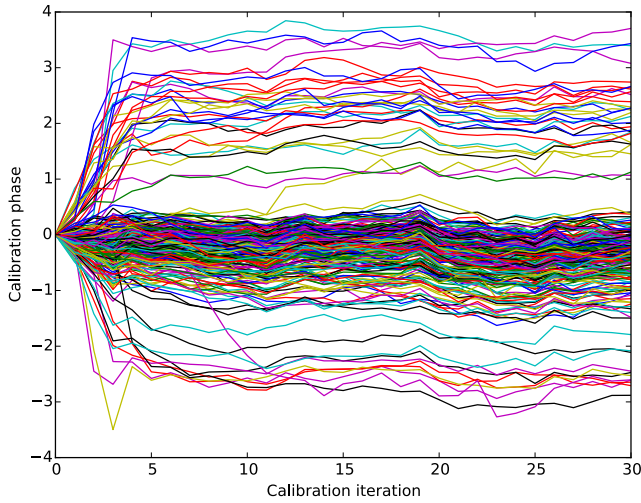


Figure 5. Gain phase solutions as a function of calibration iteration for an LWA TBN observation. The gain estimates are initialized with zero phase, but quickly span a 2π range, and settle into relatively flat, albeit noisy, solutions. The majority of phases congregate near zero, which is not surprising given the fairly good quality image produced from uncalibrated data.

ter about 15 iterations (modulo noise), and exhibit a central “trunk” where the majority of phases are congregated. This behavior is suggestive that while the uncalibrated voltages were able to produce a viable image, the minor changes from our solutions will focus the image and improve the quality. The actual location of the “trunk” (slightly negative) is simply determined by the reference antenna chosen to have identically zero phase, but happens to be slightly more positive than the bulk of antennas. For plotting clarity, we unwrapped phases resulting in phases that appear to exceed $\pm\pi$.

The gain amplitudes as a function of calibration iteration are shown in figure 6. There is a fairly wide range in gain amplitudes (from 0.12 to 0.59). However, this is not surprising due to the non-uniformity in the cables from the antennas to the receivers. Again, the amplitudes are noisy but relatively flat.

Figure 7 shows the improvement in the images due to our calibration. The left panel shows the uncalibrated image integrated over 51.2 ms, 29 kHz. Cyg A is prominent near the center of the image, and Cas A is also clearly visible in the upper right. The middle panel shows the image produced after calibration with identical integration time and bandwidth. The sidelobes (**or is it better to call them speckles due to uncalibrated phases because sidelobes are typically associated with the psf and not with calibration?**) throughout the image are significantly suppressed, and the galactic plane is much more evident, despite only modeling Cyg A and Cas A. We also note that the feature just to the right of Cyg A is dimmer in the calibrated image, better matching the expected flux from the global sky model (GSM, de Oliveira-Costa et al. 2008). We show the GSM modulated by two factors of the LWA **power pattern** in the right panel of figure 7 for reference.

To compare the image qualities quantitatively we compute the dynamic range, defined as the peak of the image over the noise level. We estimate the noise level as the median of the absolute deviation of the image, a **robust statistic**. With this metric we find the calibrated image to have a 55% dynamic range improvement over the uncalibrated image.

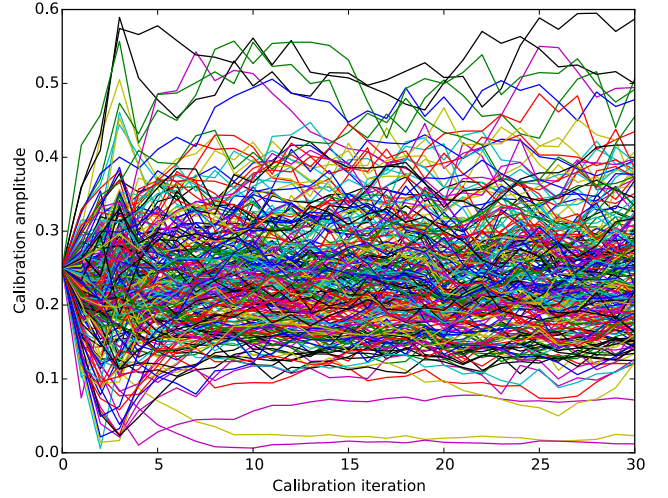


Figure 6. Gain amplitudes as a function of calibration iteration for an LWA TBN observation. The gains estimates were initialized with amplitude 0.25 after inspection of the electric field values compared to our model sky. The solutions are noisy, but flat. The range in amplitudes is due to the non-uniformity of cables between the LWA antennas and receivers.

5 NOISE TRENDS

Here we study the properties of our calibration solutions with respect to noise in the system, and compare to solutions found from visibilities. For this comparison we run a suite of simulations varying the receiver noise and integration times, while forming antenna-pixel correlations, $C_{a,s_0}^{(n)}$, for EPICal gain solutions, and simultaneously forming visibilities from the same E-field streams to find visibility-based gain solutions.

We use a simulated sky consisting of a 5 Jy calibrator source, and 10 other random sources with apparent flux densities 0.2 to 0.5 Jy (total sky power ≈ 8 Jy). We generated these sources randomly, but kept them fixed for each run. As in section 3, we use the MWA core layout (51 antennas), and a 4.4 m square tophat antenna voltage pattern. We simulate 64 40 kHz frequency channels. Because our calibration loop treats frequency channels independently, each channel can be treated as a separate trial of the simulation, and is used to better estimate the statistics.

To simulate receiver noise, we add a gaussian distributed complex random number to each antenna electric field measurement at each time stamp according to equation 3. The level of the receiver noise, $\sigma_r = \langle |\bar{n}_a(f, t)|^2 \rangle$, is varied in different simulation runs.

We initialize our gain estimates with the true values ($g_a^{(0)} = g_a^T = 1$), and allow the estimate to be corrupted by the noise through one iteration of the calibration loop. Ideally we would use a damping factor of zero to allow for the noise to fully corrupt the gains. However, we found that a zero damping factor resulted in non-convergent results, so we adopted a small factor, $\gamma = 0.05$. For a fair comparison, we use the same factor for the visibility-based solutions. We then observe the error in the gain estimates introduced by the noise.

$$\sigma_g = \left[\frac{1}{N_f N_a} \sum_f \sum_a \frac{|g'_a(f) - g_a^T(f)|^2}{|g_a^T(f)|^2} \right]^{1/2} \quad (17)$$

We simultaneously form simulated visibilities by correlating all pairs of antenna E-field measurements (including the receiver

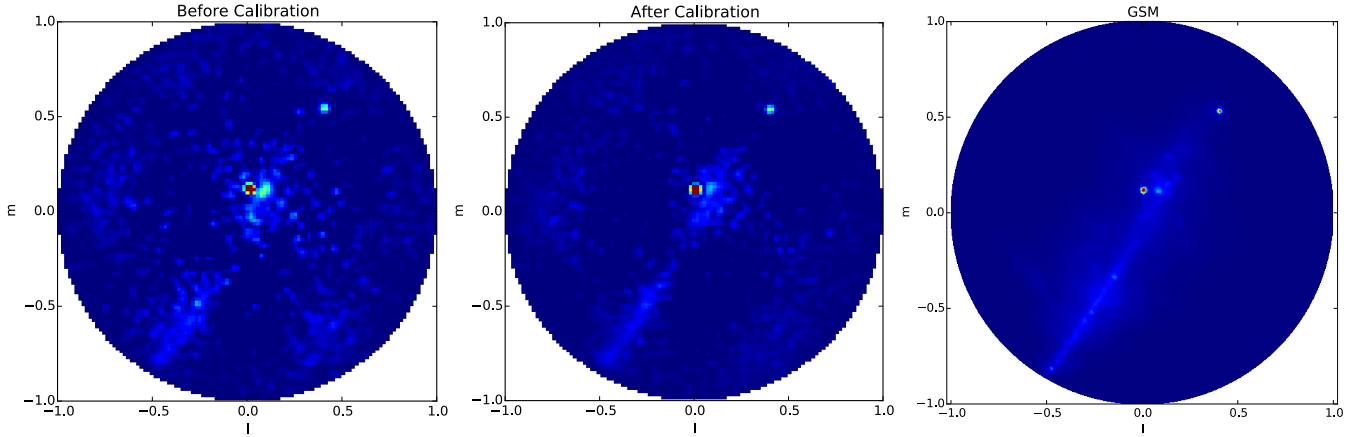


Figure 7. Images produced before (left) and after (middle) calibrating LWA data. These images were produced with 29 kHz bandwidth and 51.2 ms integration. The calibrated image shows significant reduction in sidelobe rumble throughout, while retaining the prominent Cyg A and Cas A sources. The galactic plane is also substantially more evident after calibration. For reference, the GSM is shown in the same coordinates and weighted by two factors of the LWA primary beam in the right panel. While much of the GSM is visible in the calibrated image, we note that the model used to calibrate was only the two bright sources, Cyg A and Cas A.

noise). At the end of the calibration loop we find the visibility-based gain estimates by minimizing

$$\chi^2 = \sum_a \sum_{b \neq a} |\tilde{v}_{ab} - g_a g_b^* \tilde{v}_{ab}^T|^2. \quad (18)$$

The error of the visibility-based gains is estimated in the same way as in equation 17.

The results of our simulations are shown in figure 8. The gain errors from our EPICal method is shown with solid lines, each color representing different levels of receiver noise. Each data point represents a separate simulation run (independent realization of the noise). The general trends are consistent with expectations – decreasing as the square root of integration time, and increasing with receiver noise. The lowest receiver noise level (1.0 Jy) is significantly below the sky noise contribution (about 8 Jy), so the black line is not as low, compared to the red, as one would expect from receiver noise consideration alone.

The dashed lines in figure 8 represent the errors from the visibility-based calibration. Each data point corresponds to the same simulation run as the corresponding EPICal point (same realization of noise). Generally we see the visibility-based calibration achieves slightly lower noise solutions. On average the EPICal errors are 1.5% higher, and at the worst is 3.5% higher.

We repeated this process for two extremes – a simple sky model of a single point source, and a more complicated sky with 50 sources. In the simple sky case, we found the EPICal and visibility gain estimates to be identical to floating point precision, as expected from our discussion in section 2. In the more complicated sky case (about 23 Jy total sky power), we saw the EPICal gains exhibit errors 20% higher than the visibility derived gains. The trend of higher EPICal errors with more complicated skies is due to the single correlated pixel not containing the full signal to noise of the data. This reaffirms our intuition that using a pixel with a bright source is ideal, but will still not match visibilities for complicated skies. We suggest additional strategies for improving this signal to noise in the following section.

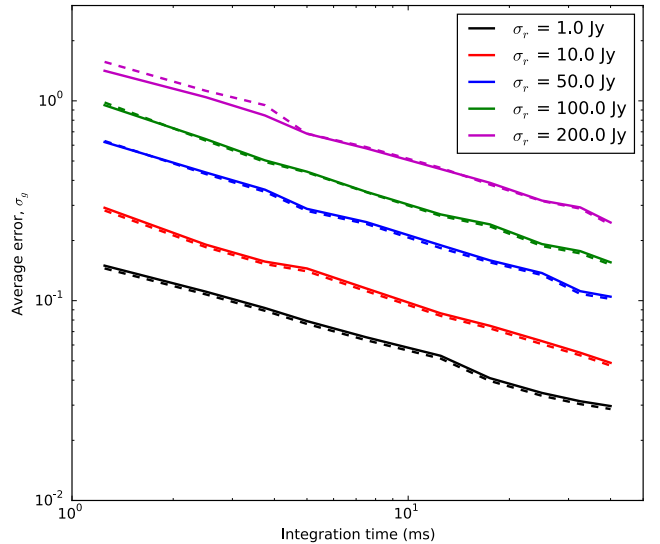


Figure 8. Gain estimate errors as a function of integration time and receiver noise (line color). The solid lines represent the error on the EPICal derived gain estimates, while the dashed lines represent the error on the visibility based estimates. On average the EPICal error is 1.5% higher than visibilities, and at worst it was 3.5% higher.

6 DISCUSSION

Through simulations and application to real data, we have shown that the EPICal algorithm is a viable solution for calibrating direct imaging arrays in real time. The computation necessary only scales with the number of antenna elements, making it a sub-dominant cost factor when designing the correlator. This strategy will enable fast read-out and arrays with many thousands of antennas, which will be necessary for future radio transient and cosmology experiments respectively.

There remain many avenues of future work before EPICal can be deployed on an instrument. Here we name a few potential

considerations for further study. These topics can be thought of as extensions to the white “estimate gains” box in figure 1, which can be performed at a much lower cadence than the actual correlations.

Fitting gain models. With some knowledge of the instrumental bandpass, the signal-to-noise of the gain solutions can be greatly improved by fitting a model to the per-frequency solutions derived here. We used this method at a rudimentary level in our demonstration to LWA data by assuming the gains were constant over a narrow bandwidth. One could easily improve on this by extending the bandwidth and fitting for a low order polynomial in phase and amplitude. Additionally, with knowledge of the poly-phase filters applied to the data stream, we could include channels closer to the edge of the band.

Improving sky model. In this work we used a perfect sky model (for simulation), or a very simple sky model (for LWA data). In principle the images produced by the EPIC correlator can be used to improve the sky model used in calibration – similar to a major loop in self-calibration. This can be especially useful for compact, widefield arrays which require a model of both compact and diffuse sources over a large patch of sky. In addition to requiring the sky model, the calibration also requires this model to be attenuated by the primary beam, which can be difficult to measure at the precision necessary (e.g. [Neben et al. 2015](#); [Virone et al. 2014](#); [Thyagarajan et al. 2015b](#)). However, the direct imaging correlator provides exactly the model necessary in real time, and can be iterated over to improve the images and gain solutions.

Dynamic parameters. In our controlled experiments we fine tuned a number of parameters based on our testing (e.g. damping factor, integration time, frequency averaging). A deployed system will require robust determination of these parameters to operate continuously. The specifics will be heavily dependent on the stability of the instrument, the frequency of observation, and the sky. For example, a stable instrument may be able to use short integrations to determine a rough estimate of the gains before switching to much longer integration (on order seconds to minutes) to highly increase signal to noise. At low frequencies or high imaging resolution, the dynamics of the ionosphere are important, and will likely drive the limit of time integration allowed.

Multiple pixel correlations. As pointed out in section 5, for a sky-noise dominated system, the signal to noise in the calibrator pixel dominates the error on the EPIC generated gain estimates. Besides the methods described above to increase signal to noise, one could also use correlations of multiple image pixels to incorporate a higher fraction of the total sky noise. Of course this increases the computational cost to a scaling of $O(N_a N_{\text{pix}})$, which will typically be much lower than the $O(N_g \log_2 N_g)$ of the correlator itself.

Direction dependent gains. Even below the timescale of a dynamic ionosphere, a widefield instrument may require direction dependent gains to account for a varying thickness ionospheric sheet. The holographic mapping framework used by the MOFF algorithm, and in turn the EPIC and EPICal software can naturally account for direction dependence through an updated model of the antenna voltage pattern. This can be achieved by using multiple pixel correlations to independently solve for gains in each pixel direction. These solutions can then be used to fit a beam model on the sky (analogous to the gain model fitting mentioned above), and updating the antenna voltage pattern. This updated pattern would then feed into the gridding step of the correlator, allowing the imager to convolve the signals with the effective beam pattern in the ground plane.

The work here will serve as a foundation for further development. We have shown that the EPICal algorithm produces reliable

calibration solutions, and have identified several aspects to increase the scope. With next generation instruments in the planning and development stages, EPICal is poised to greatly contribute to their success.

ACKNOWLEDGEMENTS

This work has been supported by the National Science Foundation through award AST-1206552. We thank Danny Jacobs for his valuable inputs, and Greg Taylor for providing us with LWA data. Construction of the LWA has been supported by the Office of Naval Research under Contract N00014-07-C-0147. Support for operations and continuing development of the LWA1 is provided by the National Science Foundation under grant AST-1139974 of the University Radio Observatory program.

REFERENCES

- Bandura K., et al., 2014, in Society of Photo-Optical Instrumentation Engineers (SPIE) Conference Series. p. 22 ([arXiv:1406.2288](#)), [doi:10.1117/12.2054950](#)
- Beardsley A. P., et al., 2012, *MNRAS*, **425**, 1781
- Bhatnagar, S. Cornwell, T. J. Golap, K. Uson, J. M. 2008, *A&A*, **487**, 419
- Bowman J. D., et al., 2013, *Publ. Astron. Soc. Australia*, **30**, 31
- Bunton J. D., 2004, *Experimental Astronomy*, **17**, 251
- Cohen A. S., Lane W. M., Cotton W. D., Kassim N. E., Lazio T. J. W., Perley R. A., Condon J. J., Erickson W. C., 2007, *AJ*, **134**, 1245
- Daishido T., et al., 2000, *Proc. SPIE*, **4015**, 73
- Ellingson S. W., et al., 2013, *IEEE Transactions on Antennas and Propagation*, **61**, 2540
- Foster G., Hickish J., Magro A., Price D., Zarb Adami K., 2014, *Monthly Notices of the Royal Astronomical Society*, **439**, 3180
- Hicks B. C., et al., 2012, *Publications of the Astronomical Society of the Pacific*, **124**, pp. 1090
- Kassim N. E., et al., 2007, *ApJS*, **172**, 686
- Lonsdale C. J., Doeleman S. S., Cappallo R. J., Hewitt J. N., Whitney A. R., 2000, in Butcher H. R., ed., Society of Photo-Optical Instrumentation Engineers (SPIE) Conference Series Vol. 4015, Radio Telescopes. pp 126–134
- Mellema G., et al., 2013, *Experimental Astronomy*, **36**, 235
- Mitchell D., Greenhill L., Wayth R., Sault R., Lonsdale C., Cappallo R., Morales M., Ord S., 2008, *Selected Topics in Signal Processing, IEEE Journal of*, **2**, 707
- Morales M. F., 2011, *PASP*, **123**, 1265
- Morales M. F., Matejek M., 2009, *MNRAS*, **400**, 1814
- Neben A. R., et al., 2015, *Radio Science*, **50**, 614
- Otobe E., et al., 1994, *PASJ*, **46**, 503
- Parsons A. R., et al., 2010, *The Astronomical Journal*, **139**, 1468
- Tegmark M., 1997, *ApJ*, **480**, L87
- Tegmark M., Zaldarriaga M., 2009, *Phys. Rev. D*, **79**, 083530
- Tegmark M., Zaldarriaga M., 2010, *Phys. Rev. D*, **82**, 103501
- Thornton D., et al., 2013, *Science*, **341**, 53
- Thyagarajan N., Beardsley A. P., Bowman J. D., Morales M. F., 2015a, [arXiv:1510.08318](#)
- Thyagarajan N., et al., 2015b, *ApJ*, **807**, L28
- Tingay S. J., et al., 2013, *PASA - Publications of the Astronomical Society of Australia*, **30**
- Virone G., et al., 2014, *Antennas and Wireless Propagation Letters, IEEE*, **13**, 169
- Wijnholds S., van der Veen A.-J., 2009, *Signal Processing, IEEE Transactions on*, **57**, 3512
- Zheng H., et al., 2014, *MNRAS*, **445**, 1084
- de Oliveira-Costa A., Tegmark M., Gaensler B. M., Jonas J., Landecker T. L., Reich P., 2008, *MNRAS*, **388**, 247
- de Vos M., Gunst A., Nijboer R., 2009, *Proceedings of the IEEE*, **97**, 1431

van Haarlem M. P., et al., 2013, [A&A](#), *556*, A2

This paper has been typeset from a \TeX/L\AA\TeX file prepared by the author.